Journal Pre-proof

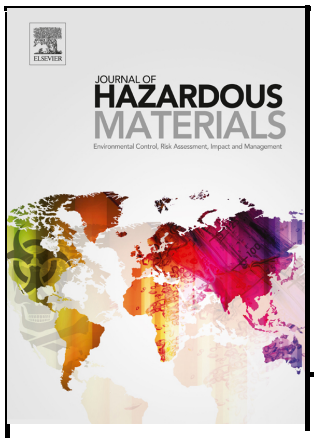

A Facile Strategy For Reclaiming Discarded Graphite and Harnessing The Rate Capabilities of Graphite Anodes

Honghong Tian, Magdalena Graczyk-Zajac, Dario M. De Carolis, Chuanmu Tian, Emmanuel III Ricohermoso, Zhiwu Yang, Wei Li, Monika Wilamowska-Zawlocka, Jan P. Hofmann, Anke Weidenkaff, Ralf Riedel

PII: S0304-3894(22)02401-3

DOI: https://doi.org/10.1016/j.jhazmat.2022.130607

Reference: HAZMAT130607

To appear in: *Journal of Hazardous Materials*

Received date: 12 October 2022
Revised date: 29 November 2022
Accepted date: 12 December 2022

Please cite this article as: Honghong Tian, Magdalena Graczyk-Zajac, Dario M. De Carolis, Chuanmu Tian, Emmanuel III Ricohermoso, Zhiwu Yang, Wei Li, Monika Wilamowska-Zawlocka, Jan P. Hofmann, Anke Weidenkaff and Ralf Riedel, A Facile Strategy For Reclaiming Discarded Graphite and Harnessing The Rate Capabilities of Graphite Anodes, *Journal of Hazardous Materials,* (2022) doi:https://doi.org/10.1016/j.jhazmat.2022.130607

A facile strategy for reclaiming discarded graphite and harnessing the rate capabilities of graphite anodes

Honghong Tian[a]*, Magdalena Graczyk-Zajac[a,b]*, Dario M. De Carolis[a], Chuanmu Tian[c], Emmanuel III Ricohermoso[a], Zhiwu Yang[d], Wei Li[a], Monika Wilamowska-Zawlocka[e], Jan P. Hofmann[c], Anke Weidenkaff[f,g], Ralf Riedel[a]

[a] Dispersive Solids, Department of Materials and Earth Sciences, Technical University of Darmstadt, Otto-Berndt-Straße 3, 64287 Darmstadt, Germany

[b] EnBW Energie Baden-Württemberg AG, Durlacher Allee 93, 76131 Karlsruhe, Germany

[c] Surface Science Laboratory, Department of Materials and Earth Sciences, Technical University of Darmstadt, Otto-Berndt-Straße 3, 64287 Darmstadt, Germany

[d] Qinghai Taifeng Pulead Lithium-Energy Technology Co., Ltd., Tongan Road 139, 810021 Xining, PR China

[e] Department of Energy Conversion and Storage, Faculty of Chemistry, Gdańsk University of Technology, Narutowicza 11/12, 80-233 Gdańsk, Poland

[f] Fraunhofer IWKS, Rodenbacher Chaussee 4, 63457 Hanau, Germany

[g] Materials and Resources, Department of Materials and Earth Sciences, Technical University of Darmstadt, Alarich-Weiss-Straße 2, 64287 Darmstadt, Germany

Corresponding Authors: honghong.tian@stud.tu-darmstadt.de (Honghong Tian)

m.graczyk-zajac@enbw.com (Magdalena Graczyk-Zajac)

ABSTRACT

Graphite negative electrodes are unbeaten hitherto in lithium-ion batteries (LiBs) due to their unique chemical and physical properties. Thus, the increasing scarcity of graphite resources makes smart recycling or repurposing of discarded graphite particularly imperative. However, the current recycling techniques still need to be improved upon with urgency. Herein a facile and efficient hydrometallurgical process is reported to effectively regenerate aged (39.5 %, 75 % state-of-health, SOH) scrapped graphite (SG) from end-of-life lithium-ion batteries. Ultimately, the first cycle reversible capacity of SG1 (SOH = 39.5 %) improved from 266 mAh/g to 337 mAh/g while 330 mAh/g (98 %) remain after 100 cycles at 0.5 C. The reversible capacity for the first cycle of SG2 (SOH = 75 %) boosted from 335 mAh/g to 366 mAh/g with the capacity retention of 99.3 % after 100 cycles at 0.5 C, which is comparable with the benchmark commercial graphite. The regenerated graphites RG1 and RG2 exhibit excellent output characteristics even increasing the rate up to 4 C. This is the best rate level reported in the literature to date. Finally, the diffusion coefficient of Li ions during deintercalation and intercalation in the regenerated graphites have been measured by

galvanostatic intermittent titration technique (GITT), determining values 2 orders-of-magnitude higher than that of the spent counterparts. Taking advantage of the synergistic effect of acid leaching and heat treatment, this strategy provides a simple and up-scalable method to recycle graphitic anodes.

Keywords:

State of health; Discarded graphite; Hydrometallurgy; Recycling; Rate-capability; Lithium-ion diffusion coefficient

1. Introduction

The development of the battery vehicle industry has been categorized as a strategic consensus of the world`s dominant economies, while simultaneously bucking the trend due to COVID-19's impact. Over the projection period of 2020 to 2025, the battery market is estimated to grow at a compound annual growth rate (CAGR) of 12.31 % [1]. By 2025 global energy storage is predicted to move into the TWh era, making it sustainably critical to fully close the waste loop as soon as possible. According to IEA analysis by 2030, roughly 100-120 GWh of power batteries used in new energy vehicles will be phased out globally each year [2-3]. The Future Waste Forecast also predicts that the cumulative end-of-life volume of electric vehicle battery modules would upsurge by 4 million tons by 2030, which is already more than the present worldwide recycling capacity [4]. Battery recycling and reusing renewable resources are essential ways to balance the demand for high penetration of renewables.

Furthermore, the Li-ion battery recycling market is fueled by the tight availability supply of raw materials utilized in lithium-ion batteries (LiBs) manufacturing, geographical resource restrictions, and strong demand in the end-use market. In terms of added value and recovery income, cathode materials are particularly sought-after due to the less profitable market of graphite. Nevertheless, we have the opposite viewpoint. Graphite cannot be replaced by other minerals due to its unique outstanding chemical and physical features, but undesirably, considering some enterprises´ indiscriminate and haphazard mining of graphite resources, the shoddy operation results in an unorganized condition of mining and processing [5]. Proven global reserves of natural graphite were around 71 million tons in 2014, but demand is steadily growing at a rate of 250000 tons per year, with approximately 72 % of graphite going into Li-ion batteries between 2016 and 2025 [6]. The established graphite resources are anticipated to become rare earth minerals or even depleted in the coming years if current mining methods and expenditures are continued. In other words, waste graphite recycling, along with prudent control and integrated planning, should not be disregarded to preserve the graphite industry's long-term survival and health. Based on the present screening and purification process for graphite electrode in used LiBs, the cost of recycled graphite is projected to be 3000 dollars per ton. Predominantly, the market price of fresh graphite ranges from 8000-13000

dollars per ton which makes waste graphite stream recycling still a considerable value embedded in manufactured LiBs for new rounds, particularly for those countries that rely heavily on graphite imports [7-8].

In the waste management hierarchy of reuse, recycling and recovery (3R concept) for graphite, there is no especially well-established research and development path, and many efforts have been made by scientific teams. Rothermal et al. treated spent graphite with a subcritical CO_2 achieving a regenerated graphite capacity up to 380 mAh/g after 50 cycles at 0.5 C [9]. Liu et al., who utilized microwave stripping and water leaching under the CO_2 process achieved an initial discharge specific capacity and coulombic efficiency of the regenerated graphite of 435.2 mAh/g and 80.6 % at 0.1 C, respectively [10]. Traditionally, pyrometallurgy requires strict ultra-high temperature conditions (2400-3300 ℃). Yu et al. graphitized scrapped graphite directly at 2400-3000 ℃ [11]. Sun et al. purified waste graphite by treating it at 3000 ℃ with a combination of acids [12]. In waste lithium batteries, a combination of pyrometallurgy and hydrometallurgy procedures may help to pave the way for recycling. Wang et al. combined H_2SO_4 leaching with calcination at 1500 ℃, achieving the first discharge capacity and capacity retention of regenerated graphite equal to 349 mAh/g and 98.8 %, respectively [13]. Other acid leaching technologies, such as HCl [14-17], H_2SO_4/H_2O_2 [11, 18-19], citric acid $C_6H_8O_7$ [20], and H_3BO_3 [21], improved the characteristics of used graphite to varying degrees.

Inspired by the above insights, in this work, the spent graphite (SG, from spent Samsung SDI cell produced in 2007) was treated using concentrated sulfuric and nitric acid and thermally annealed at 900 ℃ to obtain the regenerated graphite (RG). It is shown that the properties of the regenerated graphite are close to that of a commercial unspent graphite. The uniqueness of this approach compared to reported methods consists in three important factors which ensure a facile and efficient synthesis, namely (i) the use of cheap sulfuric and nitric acid as oxidizing and intercalating agents instead of expensive potassium permanganate, potassium perchlorate and other oxidizing agents, (ii) direct heat-treatment (<1000 ℃) and (iii) the absence of any carbon coating (glucose, pitch, phenolic resin, etc.) on the surface of the regenerated graphite, thus providing a potential future option for the up-scalable commercial recovery of scrapped graphite. **Fig. 1** shows a schematic representation of the procedure. Interestingly, the treatment with a concentrated acid mixture enhances the layer spacing of the regenerated graphite and speeds up Li^+ migration during the charging and discharging processes. The state of health (SOH) of a battery pack is a key indicator for measuring and diagnosing its aging and capacity decay. Therefore, herein systematical electrochemical investigations of two comparative SOH (39.5 % and 75 %) of spent cells accompanied by other analytical techniques are performed and evaluated.

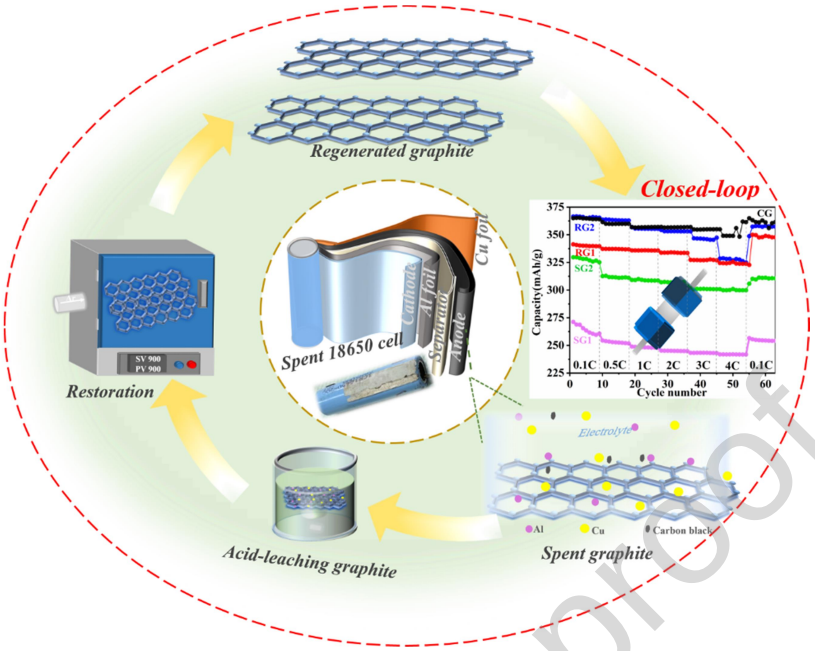

Figure 1. Schematic illustration of the regeneration process of graphite from spent Samsung LiB pack. (A color version of this figure can be viewed online.)

2. Experimental section

2.1 Materials and reagents

Sulfuric acid (H_2SO_4, AR grade, 98 %), nitric acid (HNO_3, AR grade, 65 %) were provided by Bernd Kraft. Sodium chloride (NaCl, ACS grade, 99.5 %) was purchased from VWR Chemicals. N-methyl-2-pyrrolidone (NMP, Biotech. grade, ≥ 99 %), dimethyl carbonate (DMC, Biotech. grade, ≥ 99 %), ethanol (AR grade, 95 %) and commercial natural flake graphite powders (CG, 325 mesh, ≥ 99.8 %, as a benchmark) were purchased from Alfa Aesar. Carbon black was purchased from Timcal Ltd. Carbon nanotubes (CNTs, 8-15 nm, ≥ 99.9 %) were used from Nanjing XFNANO Materials Tech Co., Ltd. Metallic Li foil (0.75 mm thickness) was bought from Alfa Aesar. A porous Whatman^{TM}-glass fiber membrane (14 mm diameter) was used as separator. A $LiPF_6$ in EC:DEC=1:1 Vol% with 10.0 % electrolyte was purchased from Xiamen TOB New Energy Technology Co., LTD. Carboxymethylcellulose (CMC) was obtained from Sigma-Aldrich, styrene butadiene rubber (SBR) from ZEON. All samples and reagents were used directly without additional purification.

2.2 Preprocessing of spent graphite

Four standard 18650 cylindrical lithium-ion power cells (2 Ah, blue cells) from Samsung pack originating from old PC designated as #3, #4, #5, and #6 in turn to facilitate identification were tested to determine their SOH. **Fig. S1 (a-c)** describes detailed information on these cells that were utilized.

Subsequently, the full cells were immersed in a 5 % NaCl solution overnight to discharge by passivating the electrode materials, water leached, and dried at room temperature. To recover the anode material, the cells were manually disassembled in Glove Box. The negative electrode materials of cells #3 and #4 revealed a similar SOH (average SOH=39.5 %) and were combined as sample 1 as well as cells #5 and #6 revealed a similar SOH (average SOH=75 %) as sample 2. The spent anode strips from sample 1 and sample 2 were then cut into small pieces of approximately 4 cm * 4 cm and stirred in ethanol at high speed for 2 h, respectively, to strip the electrode material off the copper foil. This material was filtered, and dried at 80 ℃ to obtain scrapped graphite 1 (denoted as SG1) and scrapped graphite 2 (denoted as SG2). Then SG1 or SG2 were soaked in NMP solvent and DMC solvent respectively to further eliminate the binder polyvinylidene fluoride (PVDF) and residual electrolyte, filtered, washed, and dried, and then heated at 450 ℃ for 2 h to eliminate residual binder and electrolyte decomposition products via gasification to obtain samples SG1-S and SG2-S.

2.3 Preparation of acid leaching graphite

Specifically, 2 g SG1-S or SG2-S were purified in the mixed acid (H_2SO_4:HNO_3=4:1) respectively, with a solid-liquid ratio of 1:6. The combined solution was reacted in a water bath at 95 ℃ for 4 h to dissolve the metal impurities. Afterward, the remaining solid was filtered and washed with deionized water and ethanol until the pH of the filtrate became neutral. The filter residue was dried overnight at 80 ℃ to produce acid leaching graphite, AL1 and AL2.

2.4 Preparation of regenerated graphite

The as-obtained acid leaching graphite AL1 or AL2 was introduced in a quartz boat and subsequently subjected to a tubular resistance furnace at 900 ℃ for 3 h with a heating rate of 100 ℃/h under continuous argon (Ar) flow. The final regenerated graphite was ground and sieved through 350 mesh, and designated as RG1 and RG2, respectively.

3. Materials characterizations

The crystalline phases of the samples were investigated using an X-ray powder diffractometry (XRD, STOE STADIP) in the 2θ range of 5-45 °, monochromatic Mo-*Kα* radiation (λ=0.0711 nm) and a step size of 0.1 °. Raman spectra were acquired at ambient temperature with a micro-Raman spectrometer (Horiba HR800) with an argon ion laser (wavelength of 514.5 nm) as the source of excitation in air. N_2 adsorption/desorption isotherms at 77 K (Quantachrome Autosorb-3B, Boynton Beach) were analyzed by means of the Brunauer-Emmett-Teller method (BET) and the Barrett-Joyner-Halenda algorithm (BJH) was employed to determine the specific surface area and pore size distribution of the samples. Scanning electron microscopy on a JEOL JSM 7600F (SEM, JEOL Ltd.,

Chiyoda, Tokyo, Japan) with an accelerating voltage of 15 kV with an energy dispersive spectrometer (EDS) was conducted to characterize the particle sizes, morphology, and to perform and elemental mapping analysis of the materials. In order to do the XPS measurement, the powder sample is first be sandwiched between two sheets of indium foils, then compress the indium foil so that the sample is fixed on the indium foil, and finally remove the top layer of indium foil. The X-ray photoelectron spectroscopy (XPS) was performed with a hemispherical energy analyzer (PHOIBOS 150, Focus 500 with XR50M) at a pressure $<10^{-9}$ mbar and monochromatized Al *Kα* line (1486.74 eV) was utilized as the X-ray source. The survey spectra were recorded with a pass energy of 20 eV and detailed spectra were recorded at 10 eV. The binding energy calibrated by the core lines of copper, silver, and gold, peaks were fitted by CasaXPS software using a Shirley background. The carbon content of the different samples was determined using a LECO C-200 (LECO Instrumente GmbH, Mönchengladbach, Germany). The thickness of electrode material was measured by Bruker Nano Surfaces Division with the DektakXT stylus surface profiler. Galvanostatic cycling tests of the cells were performed by discharging (Li^+ intercalation) and charging (Li^+ deintercalation) on a Neware multichannel battery tester using the BTSDA software version 7.6.0.231. The Neware equipment was used to perform a galvanostatic intermittent titration technique (GITT). Cyclic voltammetry (CV) and electrochemical impedance spectroscopy (EIS) were carried out on a Bio-Logic SP-150 cycler using the EC-Lab software version 11.36.

4. Electrochemical test

Electrochemical experiments were realized in Swagelok type cells using lithium metal foil as the counter electrode. The electrodes were fabricated by casting homogeneous slurries containing graphite (91 wt%), carboxymethylcellulose (CMC, 1.5 wt%), carbon black (2.4 wt%), carbon nanotubes (CNTs, 0.1 wt%) and styrene butadiene rubber (SBR binder, 5 wt%) on a copper foil collector, drying overnight at 40 ℃ in air to remove the residual solvent, and punched it into 10 mm circular electrodes, weighed, and further dried under vacuum conditions for 24 h at 80 ℃. The loading mass of electrodes was about 5 mg/cm^2. The electrolyte consisted of 1.0 M $LiPF_6$ in a 1:1 volume ratio mixture of ethylene carbonate (EC) and diethyl carbonate (DEC) with 10.0 wt% fluoroethylene carbonate (FEC). All the cells were galvanostatically discharged and charged at various current densities in a voltage range of 0.01-2.0 V. For the first three cycles, a constant current of 0.1 C (1 C = 372 mAh/g) was employed, and a rate of 0.5 C was applied for the following cycles. After that, the cells were evaluated at rates of 0.1 C, 0.5 C, 1 C, 2 C, 3 C, 4 C, and 0.1 C from 2.0 V to 0.01 V. CVs were performed with a sweep rate of 0.1 mV/s in the same potential range from 0.01 to 2.0 V versus Li/Li^+. EIS was measured for electrodes in the open circuit voltage (OCV) condition in the frequency range of 100 kHz to 0.1 Hz with a perturbation amplitude of 5 mV. The GITT was measured subjecting the cells to a 20 min galvanostatic discharge pulse (0.1 C), followed by a 2 h relaxation

period during which no current was transmitted through the cells. The cells were subjected to a discharge pulse followed by a relaxation time without any current flowing through the cell until its voltage reached 0.01 V vs Li/Li^+. The cells were then charged for 20 min at 0.1 C, followed by a 2 h relaxation period with no current flowing through them, repeating this sequence until its voltage increased to 2.0 V vs Li/Li^+. Five discharging-charging cycles from 0.01 V to 2.0 V vs Li/Li^+ for GITT measurements were obtained.

5. Results and discussion

The carbon content (wt%) quantified by elemental analysis is a critical criterion for determining the purity of the graphite powder. The carbon content of the RG is much higher than that of SG due to an effective removal of impurities accumulated in used graphite after repeated charging and discharging (**Table S1**).

The XRD characterization of SG, AL, and RG are compared with commercial graphite. As displayed in **Fig. 2 (a-b)**, all samples display the strongest characteristic (002) reflection of the graphite plane located at around 2 θ = 12.1 °, demonstrating that the patterns of SG, AL, RG and CG have a well-crystallized hexagonal phase with the *P63/mmc* space group (PDF card 03-065-6212). However, the main reflections of SG are weakened to variable degrees, owing to their layered structure collapsed or twisted during the repeated de/intercalation. RG displays a slightly enhanced reflection intensity after sintering, attributing to the removal of some impurities and organics. An enlargement of the peaks near 12.1 ° are taken to show the peak displacement and the shift in interplanar spacing more clearly in **Fig. 2 (c-d).** The 2 θ of SG deviates to the right as compared to CG, indicating that the interplanar spacing of graphite expands undergoing multitude irreversible chemical changes during charging and discharging. The (002) peak of RG migrated to the left after pretreatment for impurity removal and heat treatment, indicating the graphite interplanar spacing is restored to be close to that of CG after reconstructing. The interlayer spacings, calculated according to the Bragg equation $2\, d_{002} \sin\theta = \lambda$ of AL1 (0.366 nm) and AL2 (0.366 nm) are slightly enlarged after acid leaching treatment compared to SG1 (0.365 nm) and SG2 (0.365 nm), and high heat-treatment aids in the restoration of its deteriorated crystal structure [22]. The average length of the c-axis longitudinal dimension L_c (c-axis) quantified by the (002) peaks by the Scherrer equation ($L_c = K\,\lambda/\beta \cos\theta$) increases after regeneration [23-24], compared with SG (see **Table 1** and **Fig. 3**), which can be assigned to the carbon atom lattice reconstruction [12, 23-25]. Furthermore, the number of graphene layers n was calculated by the equation $n = L_c/d$.

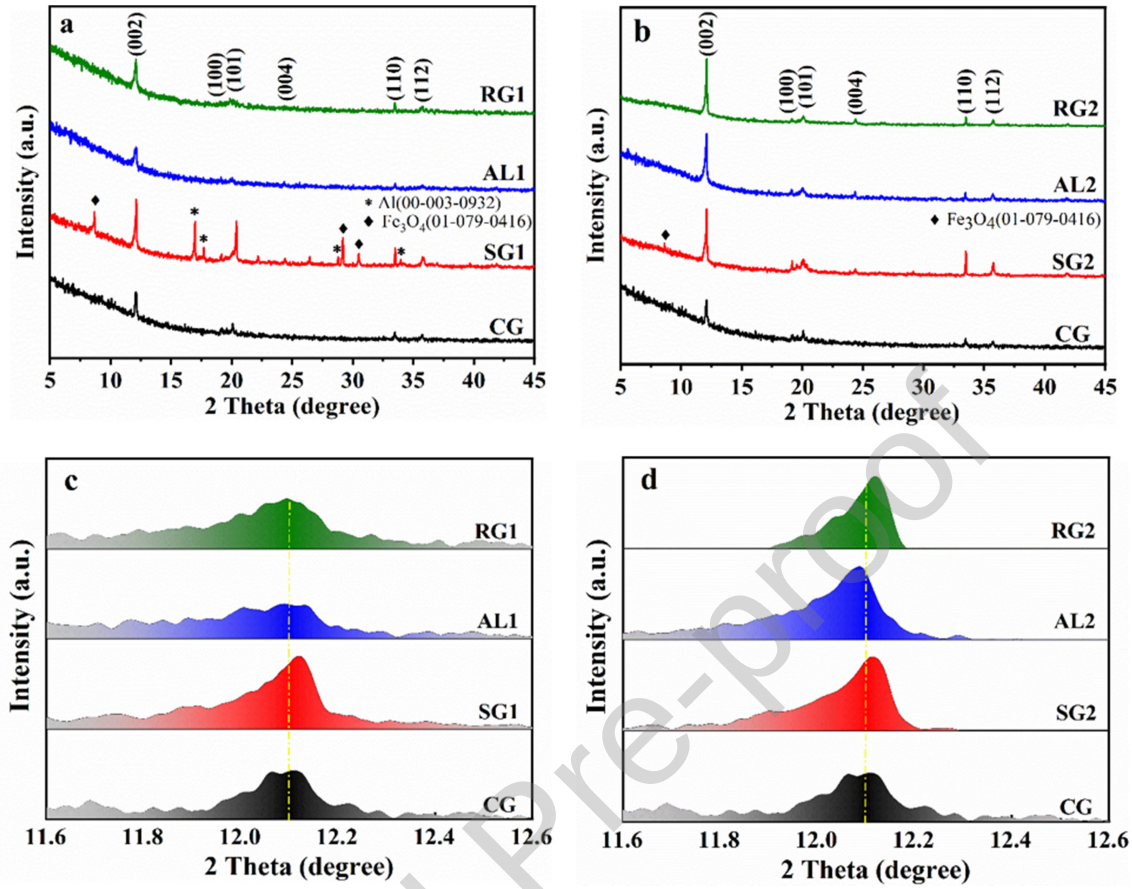

Figure 2. XRD characterization of (a) CG, SG1, AL1 and RG1. (b) CG, SG2, AL2 and RG2. (c) comparison of the (002) peak of all samples in a. (d) comparison of the (002) peak of all samples in b. (A color version of this figure can be viewed online.)

Table 1. Characteristics of CG, SG, AL, and RG at (002) plane

Sample	2 θ (°)	FWHM (cm^{-1})	Interplanar spacing (nm)	L_c (nm)	n
CG	12.06	0.00212	0.338	34.509	102
SG1	12.11	0.00197	0.365	37.032	101
AL1	12.09	0.00331	0.366	22.208	61
RG1	12.12	0.00316	0.365	23.156	63
SG2	12.12	0.00198	0.365	36.790	101
AL2	12.10	0.00238	0.366	30.743	84
RG2	12.10	0.00226	0.366	32.248	88

L_c is the size of the micro-crystallite perpendicular to the (002) interlayer plane; n is the number of microcrystallite layers; K refers to the shape factor; β is the full width at half maximum (FWHM, in radian); θ is the Bragg angle; λ is the wavelength of Mo target (0.0711 nm); d_{002} represents the interplanar spacing.

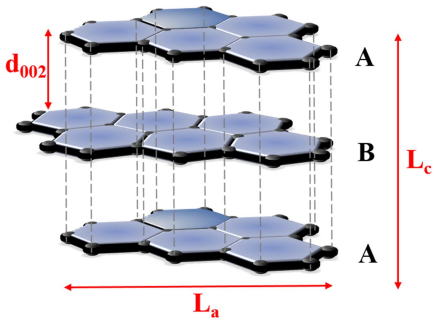

Figure 3. Hexagonal graphite layer structure and microcrystalline parameters. (A color version of this figure can be viewed online.)

Raman spectra of the investigated graphitic materials in the range from 1000 to 3000 cm^{-1} are shown in **Fig. 4 (a-b)**. Three characteristic peaks are detected in the spectra: the D band at 1357 cm^{-1} originated from the presence of disordered sp^2-hybridized carbon which causes in-plane breathing vibrations of the aromatic ring structure (A_{1g} symmetry), the G band at 1583 cm^{-1} ascribed to the in-plane stretching of sp^2 hybridized carbon (E_{2g} vibration symmetry), and the 2D band at 2721 cm^{-1}, which is the second-order peak of the D band, revealing the double vibration Raman scattering, affected by the number of graphene layers [26-27]. The defect concentration in graphitic materials can be quantified by the intensity ratio of the D band and G band (I_D/I_G parameter, peak area ratio for Gaussian fit). A general equation for the determination of lateral crystal size L_a by Raman spectra has been established as equation (1) [9, 28]. The average inter-defect distance L_D is calculated from equation (2). L_{eq} can be used from equation (3) to explain the average continuous graphene length including tortuosity [29].

$$L_a\ (nm) = (2.4 \times 10^{-10})\ {\lambda_1}^4\ (I_D/I_G)^{-1} \quad (1)$$

$$L_{D^2}\ (nm^2) = (1.8 \times 10^{-9})\ {\lambda_1}^4\ (I_D/I_G)^{-1} \quad (2)$$

$$L_{eq}\ (nm) = (77.0648)\ (I_{2D}/I_D) \quad (3)$$

The results of the analysis are summarized in **Table 2**. It shows a decrease of the crystallite sizes undergoing regenerative treatment from L_a, and the mean inter-defect distance L_D in RG lower than in SG, which can improve electrochemical performance. L_{eq}>L_a, which implies the presence of tortuosity, mainly because after concentrated acids treatment and sinter, the partial oxidation of the graphite layer edges destroys the van der Waals forces between the layers forming a very small amount of graphene [30]. The I_D/I_G of SG1 and SG2 are 0.066 and 0.146, respectively. After acid leaching and heat-treatment, the I_D/I_G of RG1 and RG2 rise to 0.256 and 0.839, respectively. This feature shows that the number of defects in RG is higher than that in SG and CG, which is due to the increased surface defects caused by the concentrated acid treatment. Thus, more active sites are exposed to provide more storage space in line with transport channels for lithium ions, improving the electrochemical performance of the electrode material. Meanwhile increased graphene layer spacing has been found, which coincides with the results obtained by XRD.

Table 2. The calculated in-plane crystallize size L_a of SG, AL, RG and CG.

Sample	D band area cm^2	G band area cm^2	I_D / I_G ratio	L_a (nm)	L_D (nm)	L_{eq} (nm)
CG	2.77	23.30	0.119	141.46	32.57	728.08
SG1	1.52	22.93	0.066	253.70	43.62	1280.19
AL1	1.62	23.74	0.068	246.44	42.99	1049.41
RG1	6.69	26.09	0.256	65.58	22.18	370.46
SG2	3.39	23.20	0.146	115.09	29.38	451.02
AL2	11.03	24.07	0.458	36.70	16.59	178.44
RG2	25.56	30.46	0.839	20.04	12.26	83.28

L_a denotes in-plane crystallinity size, nm; L_D denotes the average inter-defect distance, nm; L_{eq} denotes average continuous carbon precipitate size, nm; I_D/I_G denotes the intensity ratio of the D band and G band; I_{2D} denotes the intensity of the 2D band; λ is the laser wavelength, 514.5 nm.

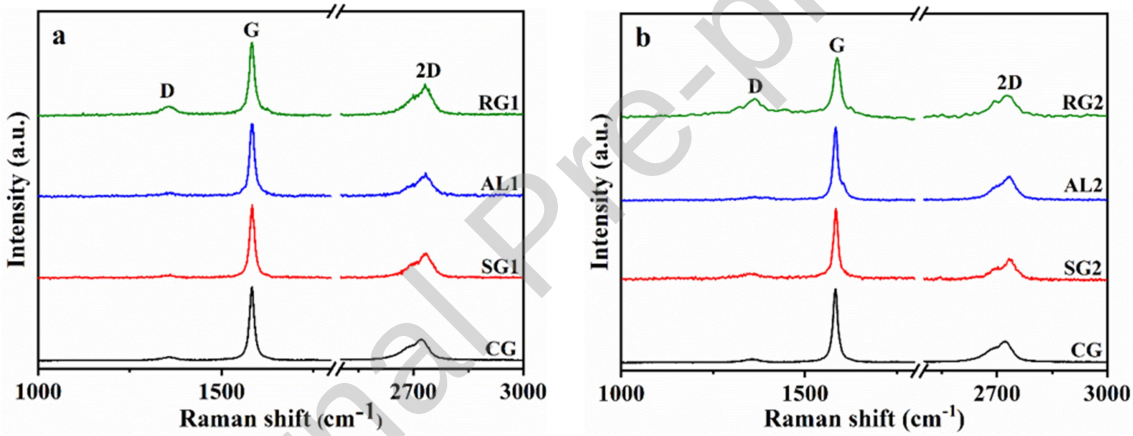

Figure 4. Raman spectra of (a) CG, SG1, AL1, and RG1. (b) CG, SG2, AL2, and RG2. (A color version of this figure can be viewed online.)

XPS measurements are performed to investigate the chemical composition of the surface of SG and RG. As shown in **Fig. S2 (a-b)**, apart from common elements C and O, the XPS full spectrum of the SG1 and SG2 show a minor F 1s peak and a Cu 2p peak. This finding indicates that the surface of the SG contains residues of electrolyte decomposition products and Cu from the collector copper foil. In RG1 and RG2, the peaks of Cu 2p and F 1s disappear when compared to SG1 and SG2 as seen in **Fig. 5 (a-b)**. The high-resolution C 1s XPS spectra of SG are displayed in **Fig. S2 (c, e)** and the details are in **Table S2**, and they predominantly reveal the presence of seven differently bonded forms of carbon, including graphitic carbon (~284.8 eV), C-C (~284.5 eV), C-O (~286.3 eV), O-C-O (~287.9 eV), C=O (~288.8 eV), O-COOR (~290.2 eV), and organofluoride -$(CF_2CH_2)_n$- (~291.5 eV) [26]. Graphitic carbon accounts for 72.9 % and 70.8 % in SG1 and SG2, respectively, which proves that after long-term cycling, the degree of graphitization decreases. The proportion of C-sp^2 in the non-polar bonds formed by C atoms has increased to 79.8 % in RG1 and 79.8 % in RG2, proving that the degree of graphitization increased. **Fig. 5 (d, f)** shows that the fitting results of the high-resolution

O 1s XPS spectra of RG1 and RG2 mainly reveal the presence of C-O (~530.6 eV) and C=O (~532.5 eV). New peak Fe-O is also observed in the **Fig. S2 (d, g)**, this is mainly due to the involve of the iron metal shell during the disassembly of the cells, and the peak disappears in RG after acid leaching. **Fig. S2 (e, h)** exhibits the F 1s spectrum at ~686.5 eV characteristic of LiF in SG, and the organofluoride -$(CF_2CH_2)_n$- exclusively association with the removal of all the impurities from PVDF and electrolyte are greatly decreased from SG, which demonstrates that the contaminants in the electrolyte are entirely eliminated in RG.

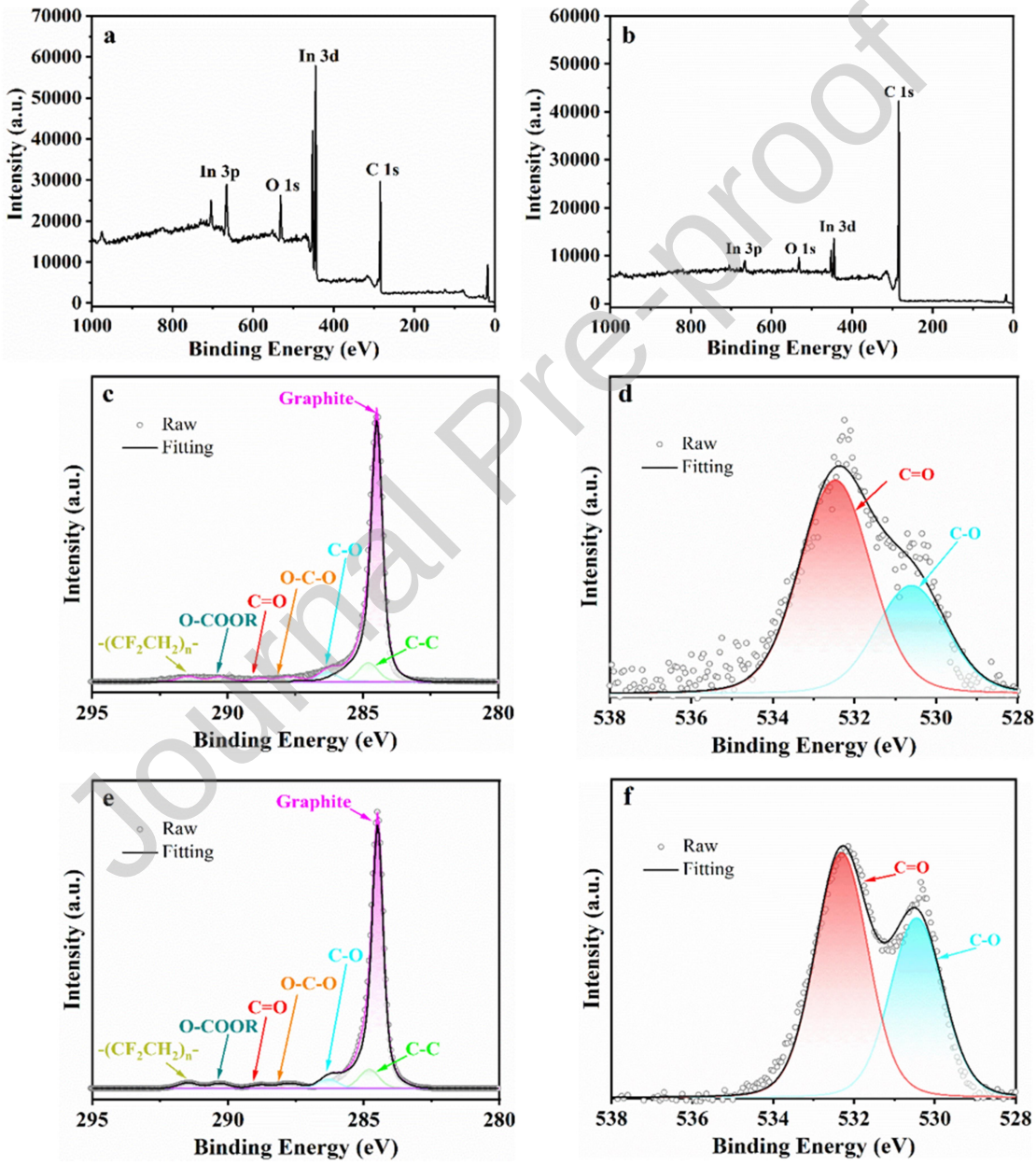

Figure 5. XPS survey spectra (a) RG1 and (b) RG2. (c) high-resolution XPS spectra of C 1s for RG1. (d) O 1s for RG1. (e) high-resolution XPS spectra of C 1s for RG2. (f) O 1s for RG2. (A color version of this figure can be viewed online.)

The nitrogen adsorption/desorption isotherms of SG, RG and CG are displayed in **Fig. 6** and **Fig. S3**. It is found that the N_2 adsorption/desorption isotherm curves of all samples are remarkably similar and exhibit typical type-IV isotherm with distinct H3 hysteresis loops induced by slit-shaped pores formed by an accumulation of flaky particles when the relative pressure approaches saturated vapor pressure and does not reach equilibrium [31]. The pore sizes are mostly spread in the range of 2-50 nm agglomerates, which corresponds to mesoporous adsorption. The results of the analyzed specific surface area (SSA) of the samples are summarized in **Table S3**. It is noteworthy mentioning that all samples show minor N_2 adsorption at a low relative pressure ($P/P_0 < 0.2$), which is attributed to van der Waals interaction between adsorbent and graphite surface. The N_2 adsorption capacity of all samples enhances considerably at high relative pressure ($P/P_0 > 0.9$), revealing a large number of large pores, which can be associated with the formation of slit-shaped pores [32]. The calculated BET specific surface area (BET SSA) of SG1 and SG2 amounts to 26.4 m^2/g and 19.8 m^2/g, respectively, while that of RG1 and RG2 decrease to 11.7 m^2/g and 12.2 m^2/g, respectively, indicating that part of the porosity on the surface of graphite has been eliminated.

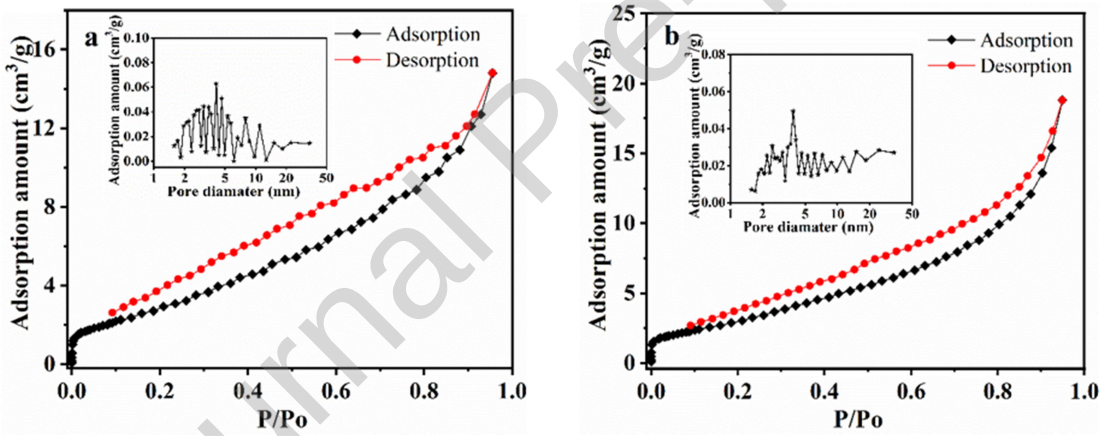

Figure 6. Nitrogen adsorption/desorption isotherms and pore size distribution (inset) of (a) RG1, (b) RG2. (A color version of this figure can be viewed online.)

SEM investigation reveals that SG1 and SG2 still retain the morphology of graphite but defects and impurities enhance the roughness of the graphite surface, as shown in **Fig. 7 (a-b)**. EDS analysis allows for determining the elemental composition of the surface. SEI film consisting of inorganic and organic materials (Li_2O, LiF, Li_2CO_3, $ROCO_2Li$, ROLi, etc.) after long-term cycling of Li-ion batteries was generated on the surface of the negative electrode, and these components are easily soluble in acid, so these impurities can also be directly removed from the graphite surface by acid leaching treatment (**Fig. S4** and **Table S4**), and then after heat-treatment, most of the impurities have been eliminated. Finally, the graphite surface in RG is much smoother than that of SG. Samples SG1 and SG2 are covered with phosphorus- and fluorine-containing impurities stemming from the electrolyte and from the collector [33]. After regeneration, RG1 and RG2 contain a low amount of

oxygen-containing functional groups, and a small amount of sulfur originate from sulfuric acid which is difficult to volatilize at high temperature (see **Fig. S5**). This finding is in accordance with the quantification of carbon as summarized in **Table 2**.

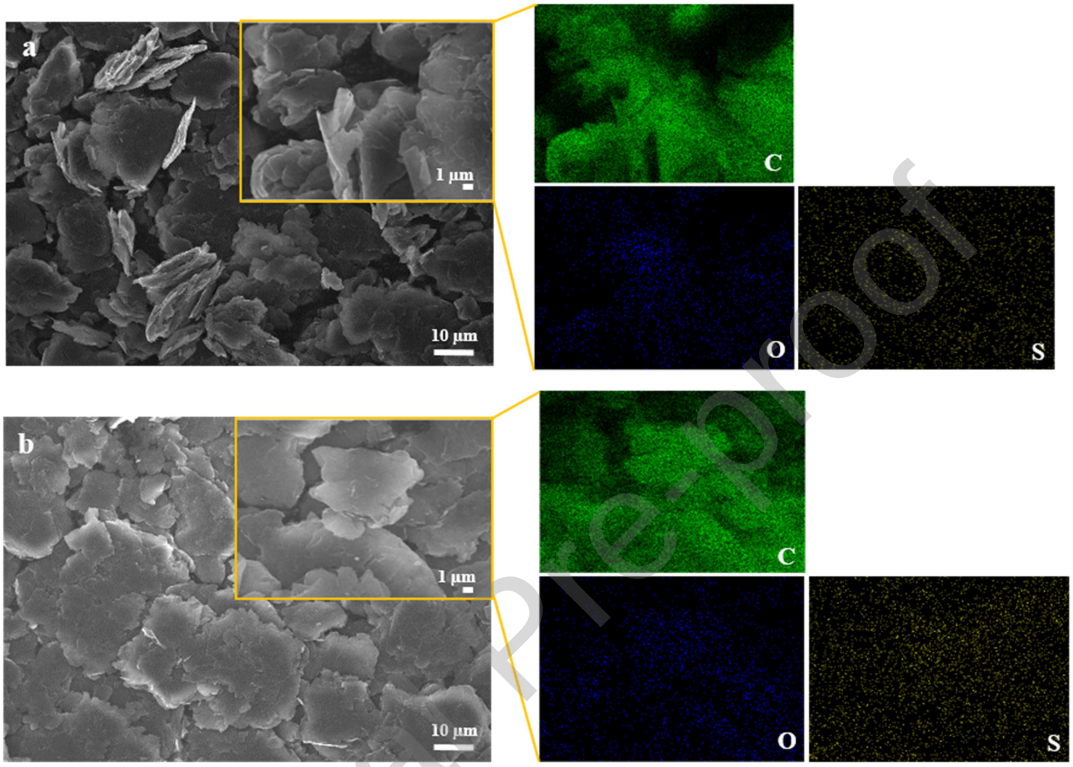

Figure 7. (a) SEM images (left) and mapping (right) of RG1, (b) SEM images (left) and mapping (right) of RG2. (A color version of this figure can be viewed online.)

Galvanostatic charging/discharging measurements were performed to evaluate the electrochemical performance of SG, RG, and CG and the results are presented in **Fig. 8 (a)**. The cells were activated after the initial three cycles at 0.1 C, followed by a long cycling period at 0.5C [34]. It is found that SG1 (SOH=39.5 %) and SG2 (SOH=75 %) show a capacity decay/instability in the first 30 cycles, and then it keeps stable during the subsequent cycles. After 140 cycles of repeated intercalation and deintercalation process, the capacity of spent graphite (SG1 274.8 mAh/g, SG2 291.7 mAh/g) is far inferior to that of commercial regular graphite. The main reason is attributed to the metal impurities introduced in waste graphite, which lead to an accelerated dissolution and regeneration of the solid electrolyte interphase (SEI) film, resulting in reduced ionic conductivity of the SEI film. Further, the metal deposits catalyze the decomposition reaction of the electrolyte, leading to a significant increase in negative interfacial impedance, resulting in loss of battery capacity and risk of battery failure. The capacity of RG1 (regenerated SOH 39.5% SG1) boosts significantly to 337.5 mAh/g on the first cycle and maintains highly reversible at 334.1 mAh/g for 120 cycles, with a

capacity retention rate of 99.0 % as shown in **Fig. 8 (b)**. The electrochemical performance of RG2 (regenerated SOH 75 % SG2) is comparable to that of CG, the first reversible capacity delivers 366.2 mAh/g and exhibits a good cycle life and 99.3 % reversibility after long-term cycling over 100 cycles. The enhanced electrochemical performance of RG2 is explained by the oxidation of acids that makes more polar functional groups appear on the surface, thus significantly increasing its surface wettability. Moreover, the increase of graphitization and reduction of structural defects, facilitates the deintercalation and intercalation of lithium ions. With respect to the 1st cycle coulombic efficiency (ICE) shown in **Table 3**, the irreversible consumption of lithium to form SEI layer for SG is substantially higher than that of RG, as it is evidenced by the CV curve shown in **Fig. 9**. These losses are directly related to a higher BET SSA of the SG materials, and the lower ICE of RG in comparison to that of CG is attributed to the presence of defects on the graphite surface.

High-rate tests of LiBs induce a mechanical stress field due to a gradient in lithium-ion concentration. It causes a gradually increasing disorder of the graphitic anode, making lithium-ion intercalation more difficult due to the existence of a new interface between the disordered particles, where lithium-ion/electrolyte reactions can occur, leading to capacity decay and lower rate performance. SG1 and SG2 demonstrate poor rate performance results as shown in **Fig. 8 (c-d)**. After regenerating, when the rate was consecutively set at the levels of 0.1 C, 0.5 C, 1 C, 2 C, 3 C, 4 C, and 0.1 C, RG1 recovered 340.1, 337.1, 335.8, 333.7, 327.2, 291.8, 335.6 mAh/g, respectively, whereas RG2 delivered 365.9, 363.3, 355.6, 353.3, 347.1, 327.4, 356.6 mAh/g, respectively, both outperforming SG1 and SG2. At low current densities (0.1 C and 0.5 C), it is comparable to CG. We rationalized this finding by shorter Li^+ migration distances in the reconstructed, but still disordered graphite, which speeds up the charge transfer. Besides, the rate capability is improved as well since the removal of bulk residual Li re-opens the channels for Li transport [21].

Table 3. First charge specific capacity, initial coulombic efficiency and capacity after 100 cycles of samples.

Sample	First charge specific capacity (mAh/g)	Initial coulombic efficiency (%)	First irreversible capacity (mAh/g)	100th charge capacity (mAh/g)
SG1	266.2	67.9	126.1	276.4
SG2	335.4	65.5	177.0	292.5
RG1	337.5	79.8	85.4	329.6
RG2	366.2	80.1	91.2	363.5
CG	363.9	82.0	79.8	359.4

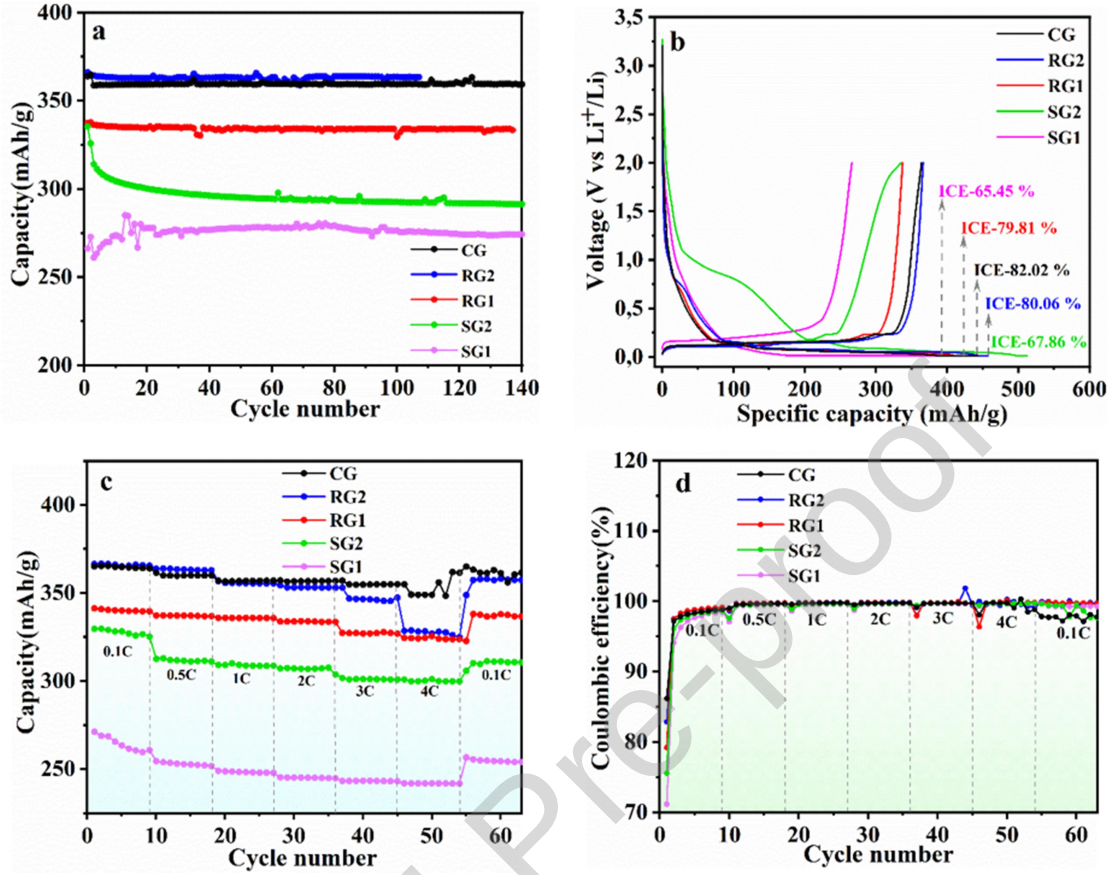

Figure 8. (a) Galvanostatic charge/discharge curves of SG1, SG2, RG1, RG2, and CG under 0.1 C for the first three cycles, and 0.5 C for the rest cycles. (b) first charge/discharge curves at 0.1 C for SG1, SG2, RG1, RG2, and CG. (c) the rate capability for SG1, SG2, RG1, RG2, and CG. (A color version of this figure can be viewed online.)

Cyclic voltammetry (CV) measurements have been carried out to examine the reduction/oxidation behavior as shown in **Fig. 9 (a-e)**. A distinct broad reduction peak is observed at around 0.64-0.75 V in the first cycle, and it disappears in the subsequent cycles, assigning to the irreversible process of the formation of SEI layer. The SEI peak of RG has a lower intensity compared to that of SG, further confirming that the regenerated graphites RG1 and RG2 have lower active surfaces available for side reactions [35]. During the reduction reaction, the cathodic peaks appeared at approximately 0.04 and 0.15 V. During the anodic scan, the oxidation takes place at about 0.24 and 0.30 V. These peaks correspond to the intercalation and extraction processes of lithium ions into graphite. They are also attributed to the typical LiC_x phase transformation [19]. On the whole, the oxidation peaks of RG and CG (see **Fig. S6**) are sharper, indicating that their reaction kinetics are faster.

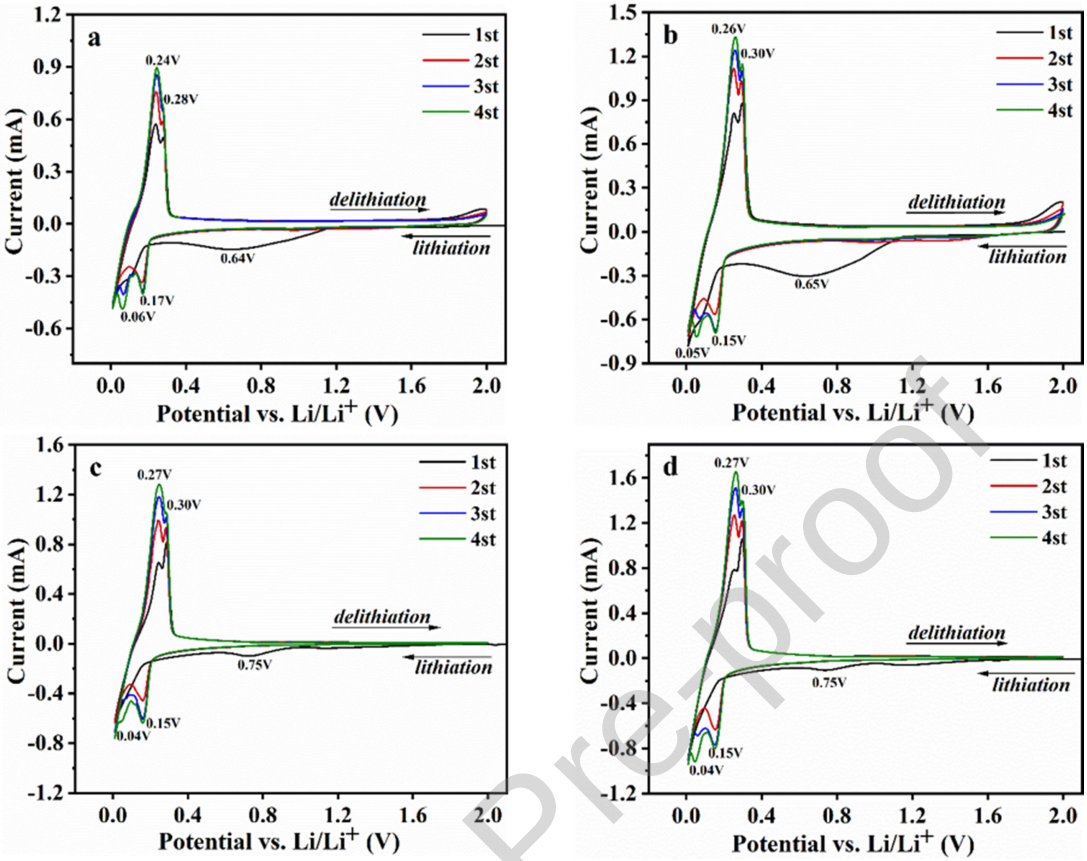

Figure 9. Cyclic voltammetry for (a) SG1, (b) SG2, (c) RG1, (d) RG2. (A color version of this figure can be viewed online.)

The electrochemical interface reaction of the electrodes was further elucidated by EIS. The obtained results approximate the lithium-ion battery to an equivalent circuit system containing resistance, inductance, and capacitance. R_b corresponds to the ohmic impedance in ultra-high frequency region, R_{sei} and C_{sei} stand for solid electrolyte impedance and capacitance in high-frequency region, R_{ct} and C_{dl} correspond to charge transfer resistance and electric double layer capacitance in middle-frequency region, and W represents the lithium-ion diffusion-controlled Warburg impedance in low-frequency region. As shown in **Fig. 10** and **Table S5**, the merging of the surface layer and charge transfer process at open circuit voltage (OCV) state is responsible for the depressed nature of the semicircle. Clearly, samples SG1 and SG2 display higher R_{sei+ct} values (41.55 Ω and 26.63 Ω, respectively) than that of RG1 (20.90 Ω) and RG2 (18.44 Ω), indicating that the electrolyte decomposition residues present on the surface of SG have been eliminated, which is favorable for the transport of lithium ions and enhanced the conductivity.

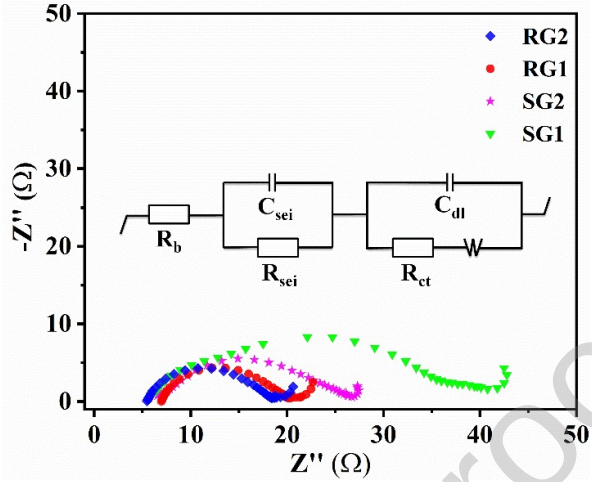

Figure 10. Nyquist plots of SG1, SG2, RG1 and RG2 electrodes at OCV condition. (A color version of this figure can be viewed online.)

To further examine the slow but critical solid-phase surface diffusion process of lithium-ion deintercalation/intercalation in the electrode materials, the GITT technique is used to record the data required for the calculation of the ion´s diffusion coefficients in the electrode material. The lithium ion diffusion coefficients are evaluated during the first cycle via GITT measurement and determined according to a simplified equation derived by Weppner et al. as follows [36-37]:

$$D = 4/\pi\tau(n_m V_m/s)^2(\Delta E_s/\Delta E_t)^2$$

D is the lithium ion diffusion coefficient, cm^2/s; τ is the relaxation time, s; n_m is the number of the moles, mol; V_m is the molar volume of the electrode material, cm^3/mol; s is the total contact area between the electrode and the electrolyte, cm^2; ΔE_s is the steady-state voltage change after the relaxation period, V. ΔE_t is the transient voltage change during the single titration current flux (after subtracting the IR drop), V.

Fig. 11 (a-b) shows the GITT curves of samples RG1 and RG2 at the first cycle in the voltage range of 0.01-2.0 V at 0.1C. The lithium-ion average apparent diffusion coefficient of RG1 and RG2 are on the order of 1.28×10^{-10} cm^2/s and 4.93×10^{-10} cm^2/s as seen in **Fig. 11 (c-d)**, respectively during delithiation and lithiation. Compared to samples SG1 (4.57×10^{-12} cm^2/s) and SG2 (9.32×10^{-12} cm^2/s), the diffusion coefficient of RG increased by 2 orders-of-magnitude as shown in **Fig. S7**. It can be concluded that the capability of reconstructed graphite to reversible Li^+ deintercalation and intercalation is improved [38], which agrees well as previously discussed in **Fig. 7(a)**.

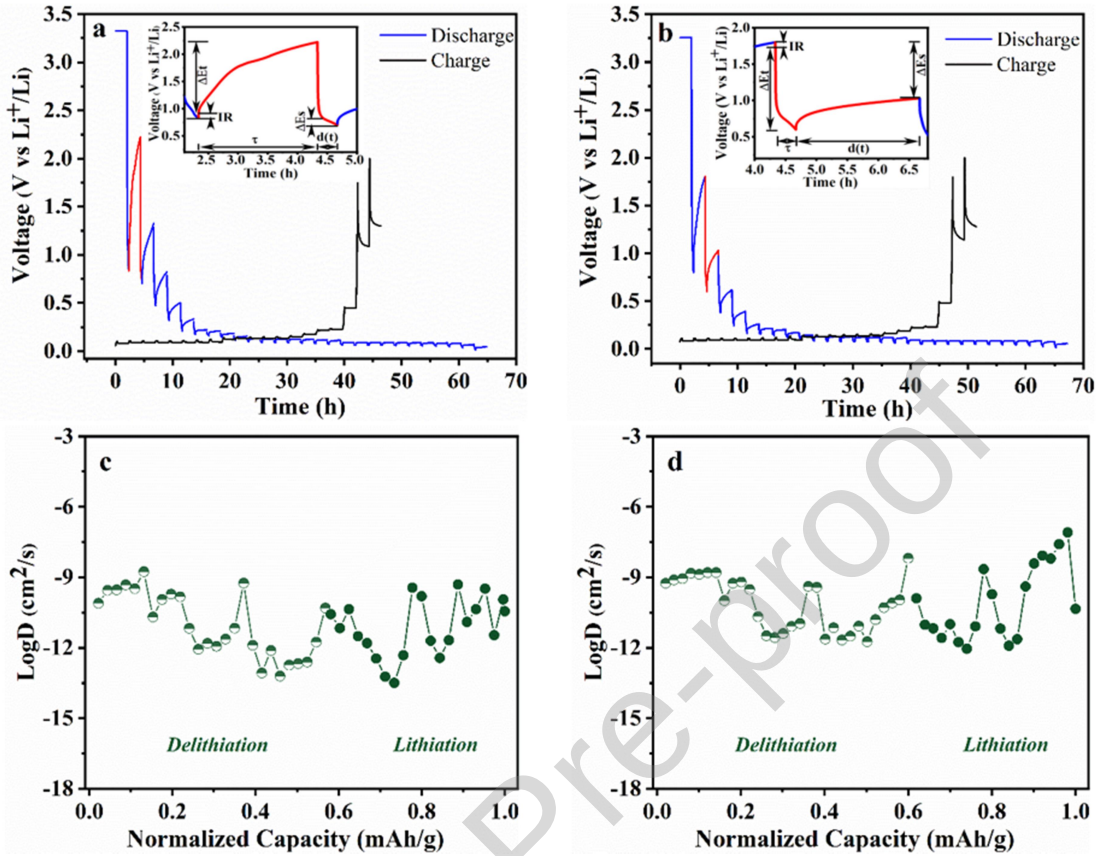

Figure 11. The current pulse vs. voltage profile at first cycle in the voltage range of 0.01-2.0 V with a schematic representation at a single step (inset shows the ''pulse + galvanostatic + relaxation'' process during discharging) (a) RG1, (b) RG2, the lithium diffusion coefficients determined from the GITT curves during charging and discharging of (c) RG1, (d) RG2. (A color version of this figure can be viewed online.)

The electrochemical performance of the recovered graphitic materials reported in the literature are listed in **Table 4** and compared to regenerated graphite RG2. RG2 recovers the highest initial reversible specific capacity and demonstrates exceptional good performance, with a capacity remaining at 353.3 mAh/g even at 4 C. The obtained performance is significantly enhanced over the results reported in the literature.

Table 4. Electrochemical performance of regenerated graphites

Recycling process	Electrode information	Electrolyte	Potential range	Reversible capacity at 1st cycle	Cycling stability	Rate capacity
HCl leaching [16]	90 % active material + 5 % AB + 5 % PVDF	1 M $LiPF_6$ in DMC:EC	0.01-2 V	591 mAh/g at 0.1 C	97.9 % after 100 cycles at 0.1 C	~ 172.6 mAh/g at 1 C
H_2SO_4+H_2O_2 leaching ─coating [6]	94.5 % active material + 1.5 % AB + 4 % PVDF	1 M $LiPF_6$ in DEC:EC	0.001-1.5 V	347.2 mAh/g at 0.1 C	98.76 % after 50 cycles at 0.1 C	~ 260 mAh/g at 2 C
Water washing [14]	80 % active material + 10 % AC + 10 % PVDF	1 M $LiPF_6$ in DEC:EC	0.005-2.5 V	~ 337 mAh/g at 0.1 C	75 % after 100 cycles at 0.2 C	~ 75 mAh/g at 2 C
HCl+H_2O_2 leaching [15]	leaching recovery of 99.4 wt% Li					
H_2SO_4+H_2O_2 leaching [38]	80 % active material + 10 % C65 +10 % PVDF	/	0.001-1.5 V	359.3 mAh/g at 0.2 C	84.63 % after 100 cycles at 0.2 C	~ 9 mAh/g at 5 C
Thermal treatment, CO_2-assisted [9]	90 % active material + 5 % SP +5 % Na-CMC	1 M $LiPF_6$ in DEC:EC	0.02-1.5 V	345 mAh/g at 0.1 C	379 mAh/g after 100 cycles at 0.5 C	/
Thermal treatment (3000 °C) ─coating [19]	94.5 % active material + 1.5 % SP +1.5 % CMC + 2 % SBR	1 M $LiPF_6$ in DMC:EC	0.005-2.0 V	324.58 mAh/g at 0.2 C	348 mAh/g after 100 cycles at 0.5 C	~ 285 mAh/g at 1 C
H_2SO_4 curing ─leaching [13]	93 % active material + 2 % AB + 5 % PVDF	1 M $LiPF_6$ in DMC:EC:EMC	0.001-2.5 V	349 mAh/g at 0.1 C	98.9 % after 50 cycles at 0.1 C	~ 45 mAh/g at 2 C
Microwave─CO_2 [10]	80 % active material + 10 % AB + 10 % PVDF	1 M $LiPF_6$	0.005-2.6 V	353.5 mAh/g at 0.1 C	320 mAh/g after 100 cycles at 0.5 C	~ 86 mAh/g at 2 C
3000 °C [11]	85 % active material + 5 % AB + 10 % PVDF	1 M $LiPF_6$ in DMC:EC	0.01-3.5 V	351.9 mAh/g at 0.1 A/g	97.42 % after 100 cycles at 0.1 A/g	/
Citric acid leaching [20]	80 % active material + 10 % AB + 10 % PVDF	1 M $LiPF_6$ in DMC:EC:EMC	0.01-2 V	468.3 mAh/g at 0.1 C	330 mAh/g after 80 cycles at 0.1 C	~ 174 mAh/g at 2 C
Boric acid leaching [21]	80 % active material + 10 % SP + 10 % PVDF	1 M $LiPF_6$ in DEC:EC	0.01-1.5 V	332 mAh/g at 0.1 C	325 mAh/g after 100 cycles at 0.1 C	~ 140 mAh/g at 1 C
Commercial graphite in our work	91 % active material + 2.4 % CB +1.5 % CMC + 5 % SBR+0.1 % CNTs	1 M $LiPF_6$ in DEC:EC + 10 % FEC	0.01-2.0 V	363.90 mAh/g at 0.1 C	359.38 % after 100 cycles at 0.5 C	~ 352.46 mAh/g at 4 C
Our work H_2SO_4+HNO_3 leaching	**91 % active material + 2.4 % CB +1.5 % CMC + 5 % SBR+0.1 % CNTs**	**1 M $LiPF_6$ in DEC:EC + 10 % FEC**	**0.01-2.0 V**	**366.20 mAh/g at 0.1 C**	**363.53 mAh/g after 100 cycles at 0.5 C**	**~ 353.27 mAh/g at 4 C**

AB, acetylene black; AC, acetylene carbon black; SP, super P; C65, a type of carbon black; DMC, dimethyl carbonate; EC, ethylene carbonate; DEC, diethyl carbonate; FEC, fluoroethylene carbonate; 1 C=372 mAh/g.

6. Conclusions and outlook

In conclusion, we have demonstrated a facile recycling perspective using simple acid treatment and thermal anneal to transform waste graphite originating from cells with two different SOH into high-performing recovered graphite. These regenerated graphites exhibit outstanding electrochemical performance in both capacity and rate performance as compared to the literature. We performed GITT technique to elaborate the solid-phase surface diffusion process during lithium ion deintercalation/intercalation in the electrode materials. We have found that the regenerated graphites provide superior electrochemical performance due to 2 orders-of-magnitude increase in the average diffusion coefficient of lithium ions.

Although the performance of re-established graphite is comparable to that of commercial graphite in all respects, the low first coulombic efficiency (RG1 79.81 %, RG2 80.06 %) restricts its widespread use to some extent, which might lead to a necessity of a prelithiation which will be addressed in our future research.

CRediT authorship contribution statement

Honghong Tian: Conceptualization, methodology, synthesis, characterization, data analytics, writing original draft. **Magdalena Graczyk-Zajac:** Conceptualization, methodology, supervision, review & editing. **Dario M. De Carolis:** Discussion, review. **Chuanmu Tian:** XPS test. **Emmanuel III Ricohermoso**: SEM test. **Zhiwu Yang:** Providing comments on the experiments. **Wei Li:** The carbon content test. **Monika Wilamowska-Zawlocka:** Review & editing. **Jan Philipp Hofmann:** XPS test, review & editing. **Anke Weidenkaff:** Review. **Ralf Riedel:** Supervision, review & editing.

Declaration of competing interest

The authors declare that they have no known competing financial interests or personal relationships that could have appeared to influence the work reported in this paper.

Acknowledgments

Honghong Tian kindly acknowledges the financial support by the China Scholarship Council (CSC, No.202009150013). Ralf Riedel, Magdalena Graczyk-Zajac and Dario M. De Carolis acknowledge the support of HA HessenAgentur GmbH, Innovationsförderung Hessen-Förderung der Elektromobilität, project number 849/20-09. Chuanmu Tian (CSC, No. 202008420222) and Wei Li (CSC, No. 201907040060) kindly acknowledge the financial support by the China Scholarship Council.

Appendix A. Supplementary data

References

[1] Y.P. Miao, L.L. Liu, Y.P. Zhang, Q.Y. Tan, J.H. Li, An overview of global power lithium-ion batteries and associated critical metal recycling, J. Hazard. Mat. 425 (2022), 1-14. https://doi.org/10.1016/j.jhazmat.2021.127900.

[2] IEA, Global EV Outlook 2020, https://www.iea.org/reports/global-ev-outlook-2020, 2020 (accessed June 2020).

[3] IEA, Global EV Outlook 2021, https://www.iea.org/reports/global-ev-outlook-2021?mode=overview, 2021 (accessed April 2021).

[4] IEA, The role of critical minerals in clean energy transitions, https://www.iea.org/reports/the-role-of-critical-minerals-in-clean-energy-transitions, 2021 (accessed May 2021).

[5] S. Natarajan, M.L. Divya, V. Aravindan, Should we recycle the graphite from spent lithium-ion batteries? The untold story of graphite with the importance of recycling, J. Energy Chem. 71 (2022), 351-369. https://doi.org/10.1016/j.jechem.2022.04.012.

[6] J. Zhang, X.L. Li, D.W. Song, Y.L. Miao, J.S. Song, L.Q. Zhang, Effective regeneration of anode material recycled from scrapped Li-ion batteries, J. Power Sources. 390 (2018), 38–44. https://doi.org/10.1016/j.jpowsour.2018.04.039.

[7] C.X. Yi, Y. Yang, T. Zhang, X.Q. Wu, W. Sun, L.S. Yi, A green and facile approach for regeneration of graphite from spent lithium ion battery, J. Clean. Prod. 277 (2020), 1-10. https://doi.org/10.1016/j.jclepro.2020.123585.

[8] W.X. Zhang, Z.P. Liu, C.J. Xu, W.Z. He, G.M. Li, J.W. Huang, H.C. Zhu, Preparing graphene oxide copper composite material from spent lithium ion batteries and catalytic performance analysis, Res. Chem. Intermed. 44 (9) (2018), 5075–5089. https://doi.org/10.1007/s11164-018-3410-4.

[9] S. Rothermel, M. Evertz, J. Kasnatscheew, X. Qi, M. Grützke, M. Winter, S. Nowak, Graphite recycling from spent lithium-ion batteries, ChemSusChem. 9 (2016), 3473–3484. https://doi.org/10.1021/acssuschemeng.0c02321.

[10] Y.W. Chao, B.G. Liu, H. Zhang, S.H. Tian, L.B. Zhang, S.H. Guo, B.C. Zhou, Efficient recovery and regeneration of waste graphite through microwave stripping from spent batteries anode for high-performance lithium-ion batteries, J. Clean. Prod. 333 (2022), 1-8. https://doi.org/10.1016/j.jclepro.2021.130197.

[11] H.J. Yu, H.L. Dai, Y. Zhu, H.W. Hu, R.R. Zhao, B.B. Wu, D.C. Chen, Mechanistic insights into the lattice reconfiguration of the anode graphite recycled from spent high power lithium-ion batteries, J. Power Sources. 481 (2021), 1-13. https://doi.org/10.1016/j.jpowsour.2020.229159.

[12] Z. Sun, H. Zheng, Y. Wang, X. Lin, H. Cao, A Method for recycling the anode materials from scrapped lithium-ion batteries, 2018, CN107887666A. 2018-09-25.

[13] Y. Gao, C.Y. Wang, J.L. Zhang, Q.K. Jing, B.Z. Ma, Y.Q. Chen, W.J. Zhang, Graphite recycling from the spent lithium-ion batteries by sulfuric acid curing–leaching combined with high-temperature calcination, ACS Sust. Chem. Eng. 8(25) (2020), 9447-9455. https://doi.org/10.1021/acssuschemeng.0c02321.

[14] I. Rey, C. Vallejo, G. Santiago, M. Iturrondobeitia, E. Lizundia, Environmental impacts of graphite recycling from spent lithium-ion batteries based on life cycle assessment, ACS Sustainable Chem. Eng. 9 (2021), 14488–14501. https://doi.org/10.1021/acssuschemeng.1c04938.

[15] Y. Guo, F. Li, H.C. Zhu, G.M. Li, J.W. Huang, W.Z. He, Leaching lithium from the anode electrode materials of spent lithium-ion batteries by hydrochloric acid (HCl), Waste Manage. 51 (2016), 227–233. https://doi.org/10.1016/j.wasman.2015.11.036.

[16] Y. Yang, S.L. Song, S.Y. Lei, W. Sun, H.S. Hou, F. Jiang, X.B. Ji, W.Q. Zhao, Y.H. Hu, A process for combination of recycling lithium and regenerating graphite from spent lithium-ion battery, Waste Manage. 85 (2019), 529–537. https://doi.org/10.1016/j.wasman.2019.01.008.

[17] Z.Q. Cao, X.H. Zheng, H.B. Cao, H. Zhao, Z. Sun, Z. Guo, K. Wang, B. Zhou, Efficient reuse of anode scrap from lithium-ion batteries as cathode for pollutant degradation in electro-Fenton process: Role of different recovery processes, Chem. Eng. J. 337 (2018), 256–264. https://doi.org/10.1016/j.cej.2017.12.104.

[18] Q.W. Zhou, Z.X. Huang, J.W. Liu, Y.F. Zhao, J.C.Y. Jung, J.J. Zhang, S.M. Xu, A closed-loop regeneration of $LiNi_{0.6}Co_{0.2}Mn_{0.2}O_2$ and graphite from spent batteries via efficient lithium supplementation and structural remodelling, Sustain. Energ. Fuels. 5 (2021), 4981–4991. https://doi.org/10.1039/D1SE01114F.

[19] D.S. Ruan, F.M. Wang, L. Wu, K. Du, Z.H. Zhang, K. Zou, X.F. Wu, G.R. Hu, A high-performance regenerated graphite extracted from discarded lithium-ion batteries, New J. Chem. 3 (2021), 1535-1540. https://doi.org/10.1039/D0NJ05434H.

[20] J.B. Yang, E.S. Fan, J. Lin, F. Arshad, X.D. Zhang, H.Y. Wang, F. Wu, R.J. Chen, L. Li, Recovery and reuse of anode graphite from spent lithium-ion batteries via citric acid leaching, ACS Appl. Energ. Mater. 4 (6) (2021), 6261–6268. https://doi.org/10.1021/acsaem.1c01029.

[21] B. Markey, M.H. Zhang, I. Robb, P.P. Xu, H.P. Gao, D.W. Zhang, J. Holoubek, D. Xia, Y.F. Zhao, J.C. Guo, M. Cai, Y.S. Meng, Z. Chen, Effective upcycling of graphite anode: healing and doping enabled direct regeneration, J. Electrochem. Soc. 167 (16) (2020). https://doi.org/10.1149/1945-7111/abcc2f.

[22] D. Gonzalez, O. Altin, S. Eser, A.B. Garcia, Temperature-programmed oxidation studies of carbon materials prepared from anthracites by high temperature treatment, Acta Cryst. 101 (1950), 137-141. https://doi.org/10.1016/j.matchemphys.2006.03.001.

[23] F.T.L. Muniz, M.A.R. Miranda, C.M. Santos, J.M. Sasaki, The Scherrer equation and the dynamical theory of X-ray diffraction, Acta Crystallogr. A: Found. Advances. 3 (2016), 385-390. https://doi.org/10.1107/S205327331600365X.

[24] Y. Gao, C.Y. Wang, J.L. Zhang, Q.K. Jing, B.Z. Ma, Y.Q. Chen, W.J. Zhang, Regenerating spent graphite from scrapped lithium-ion battery by high-temperature treatment, Carbon. 189 (2022), 493-502. https://doi.org/10.1016/j.carbon.2021.12.053.

[25] H. He, C. Huang, C.W. Luo, J.J. Liu, Z.S. Chao, Dynamic study of Li intercalation into graphite by in situ high energy synchrotron XRD, Electrochim. Acta. 92 (2013), 148-152. https://doi.org/10.1016/j.electacta.2012.12.135.

[26] Z.H. Zhang, X.D. Zhu, H.L. Hou, L. Tang, J. Xiao, Q.F. Zhong, Regeneration and utilization of graphite from the spent lithium-ion batteries by modified low-temperature sulfuric acid roasting, Waste management. 150 (2022), 30-38. https://doi.org/10.1016/j.wasman.2022.06.037.

[27] A.C. Ferrari, J.C. Meyer, V. Scardaci, C. Casiraghi, M. Lazzeri, F. Mauri, S. Piscanec, D. Jiang, K.S. Novoselov, S. Roth, A.K. Geim, Raman spectrum of graphene and graphene layers, Phys. Rev. Lett. 18 (2006). https://doi.org/10.1103/PhysRevLett.97.187401.

[28] L. G. Cançado, K. Takai, T. Enoki, M. Endo, Y.A. Kim, H. Mizusaki, A.Jorio, L.N. Coelho, R.M. Paniago, M.A. Pimenta, General equation for the determination of the crystallite size L_a of nanographite by Raman spectroscopy, Appl. Phys. Lett. 88 (2006). https://doi.org/10.1063/1.2196057.

[29] C. Stabler, A. Reitz, P. Stein, B. Albert, R. Riedel, E. Ionescu, Thermal Properties of SiOC Glasses and Glass Ceramics at Elevated Temperatures, Materials. 11 (2018), 1-20. https://doi.org/10.3390/ma11020279.

[30] N. Larouche, B.L. Stansfield, Classifying nanostructured carbons using graphitic indices derived from Raman spectra, Carbon. 48 (2010), 620–629. https://doi.org/10.1016/j.carbon.2009.10.002.

[31] K.L. Jones, G.M. Laudone, G.P. Matthews, A multi-technique experimental and modelling study of the porous structure of IG-110 and IG-430 nuclear graphite, Carbon. 128 (2018), 1-11. https://doi.org/10.1016/j.carbon.2017.11.076.

[32] M.A. Banares-munoz, L.V. Flores Gonzalez, J.M. Martin Llorenta, Adsorption isotherms of nitrogen and argon on an “agot” grade artificial nuclear graphite at 77 and 90 K, Carbon. 25 (1987), 603-608. https://doi.org/10.1016/0008-6223(87)90210-7.

[33] V Kraft, M Grützke, W Weber, J Menzel, S.W. Meyer, M Winter, S Nowak, Two-dimensional ion chromatography for the separation of ionic organophosphates generated in thermally decomposed lithium hexafluorophosphate-based lithium ion battery electrolytes, J. Chromatogr. A, 1409(2015), 201-209. https://doi.org/10.1016/j.chroma.2015.07.054.

[34] Z. Ma, Y.C. Zhuang, Y.M. Deng, X.N. Song, X.X. Zuo, X. Xiao, J.M. Nan, From spent graphite to amorphous sp^2 + sp^3 carbon-coated sp^2 graphite for high-performance lithium ion batteries, J. Power Sources. 376 (2018), 91-99. https://doi.org/10.1016/j.jpowsour.2017.11.038.

[35] E.J. McShane, H.K. Bergstrom, P.J. Weddle, D.E. Brown, A.M. Colclasure, B.D. McCloskey, Quantifying graphite solid-electrolyte interphase chemistry and its impact on fast charging, ACS Energy Lett. 7 (2022), 2734-2744. https://doi.org/10.1021/acsenergylett.2c01059.

[36] W. Weppner and R. A. Huggins, Determination of the kinetic parameters of mixed-conducting Electrodes and application to the system Li_3Sb, J. Electrochem. Soc. 124 (1977), 1569-1578. https://doi.org/10.1149/1.2133112.

[37] K.M. Shaju, G.V. Subba Rao, B.V.R. Chowdari, EIS and GITT studies on oxide cathodes, O2-$Li_{(2/3)+x}(Co_{0.15}Mn_{0.85})O2$ (x =0 and 1/3), Electrochim. Acta. 48 (2003), 2691-2703. https://doi.org/10.1016/S0013-4686(03)00317-7.

[38] X.T. Ma, M.Y. Chen, B. Chen, Z.F. Meng, Y. Wang, High-performance graphite recovered from spent lithium-ion batteries, ACS Sustain. Chem. Eng. 24 (2019), 19732-19738. https://doi.org/10.1021/acssuschemeng.9b05003.

CRediT authorship contribution statement

Honghong Tian: Conceptualization, methodology, synthesis, characterization, data analytics, writing original draft. **Magdalena Graczyk-Zajac:** Conceptualization, methodology, supervision, review & editing. **Dario M. De Carolis:** Discussion, review. **Chuanmu Tian:** XPS test. **Emmanuel III Ricohermoso**: SEM test. **Zhiwu Yang:** Providing comments on the experiments. **Wei Li:** The carbon content test. **Monika Wilamowska-Zawlocka:** Review & editing. **Jan Philipp Hofmann:** XPS test, review & editing. **Anke Weidenkaff:** Review. **Ralf Riedel:** Supervision, review & editing.

Declaration of interests

☒ The authors declare that they have no known competing financial interests or personal relationships that could have appeared to influence the work reported in this paper.

☐ The authors declare the following financial interests/personal relationships which may be considered as potential competing interests:

Environmental Implication

Faced with the increasing number of retired batteries, waste batteries discarded directly in landfills can cause heavy metal ion contamination, fluorine contamination and organic contamination, which in turn penetrates into soil and water, ultimately threatening organisms at all nutrient levels. Recycling them not only promotes the recycling of resources to achieve a closed loop to alleviate the crisis of raw material shortage. It also reduces the harm to the environment and realize the sustainable development of recycling. we have demonstrated a facile recycling perspective using simple acid-treatment and thermal annealing to transform waste graphite into high-performing recovered graphite.

Graphical abstracts

Regeneration process of graphite from spent Samsung LiB pack.

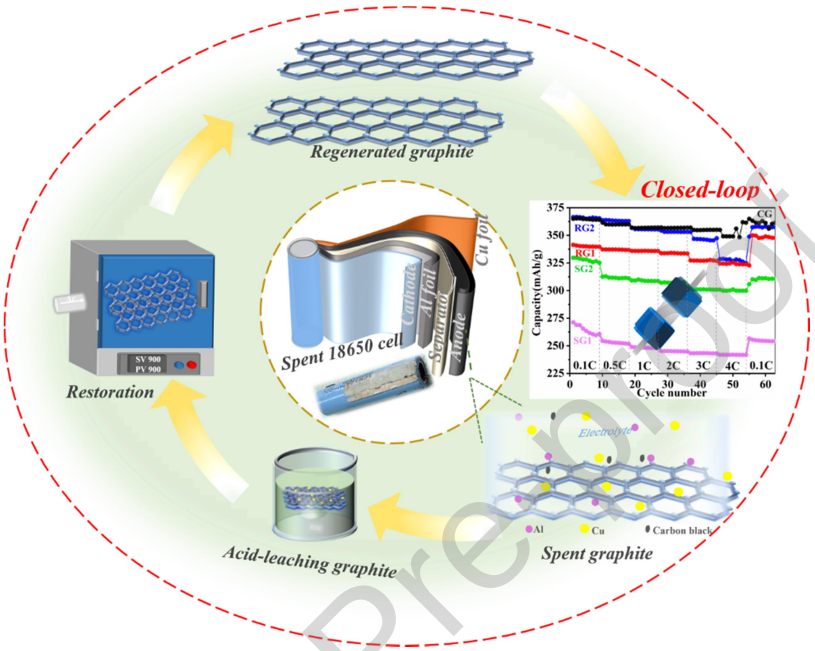

Highlights

- Two comparative SOH of spent cells are performed and evaluated.
- RG2 is as high as 366.20 mAh/g at initial, and maintains 99.27 % capacity (0.5 C) after 100 cycles.
- RGs exhibit excellent output characteristics as the C rate was boosted even at 4 C.
- The diffusion coefficient of Li ions in RGs are values 2 orders-of-magnitude higher than that of the spent counterparts.